Collisions of solitary waves in condensates beyond mean-field theory

Aparna Sreedharan,[1,*] Sarthak Choudhury,[1] Rick Mukherjee,[1,2] Alexey Streltsov,[3,4] and Sebastian Wüster[1,†]
[1]*Department of Physics, Indian Institute of Science Education and Research (IISER), Bhopal, Madhya Pradesh 462066, India*
[2]*Department of Physics, Imperial College, London SW7 2AZ, United Kingdom*
[3]*Theoretische Chemie, Physikalisch-Chemisches Institut, Universität Heidelberg, Im Neuenheimer Feld 229, D-69120 Heidelberg, Germany*
[4]*SAP Deep Learning Center of Excellence and Machine Learning Research SAP SE, Dietmar-Hopp-Allee 16, 69190 Walldorf, Germany*

(Received 6 May 2019; revised manuscript received 27 January 2020; accepted 21 February 2020; published 6 April 2020)

Bright solitary waves in a Bose-Einstein condensate contain thousands of identical atoms held together despite their only weakly attractive contact interactions. They nonetheless behave like a compound object, staying whole in collisions, with their collision properties strongly affected by intersoliton quantum coherence. We show that separate solitary waves decohere due to phase diffusion, dependent on their effective ambient temperature, after which their initial mean-field relative phases are no longer well defined or relevant for collisions. In this situation, collisions occur predominantly repulsively and can no longer be described within mean-field theory. When considering the timescales involved in recent solitary wave experiments where nonequilibrium phenomena play an important role, these features could explain the predominantly repulsive collision dynamics observed in most condensate soliton train experiments.

DOI: 10.1103/PhysRevA.101.043604

I. INTRODUCTION

Dilute alkali-metal gas Bose-Einstein condensates (BECs) can usually be well understood using a simplified model for atomic collisions based on contact interactions and further employing a product mean-field ansatz where all particles reside in the same single particle state to vastly simplify the quantum many-body physics [1,2].

Here we explore why the mean-field approach breaks down in collisions of bright matter-wave solitary waves [1,3,4], which are self-localized nonlinear wave packets containing thousands of condensate atoms. Bright solitary matter waves in Bose-Einstein condensates have now been created in a variety of experiments [4–18], for fundamental studies and applications in interferometry. We use "solitary wave" here to imply that the three-dimensional character of the wave function was still relevant in all these experiments. In the remainder of the article, we shall also use the shorthand "soliton." In many of these experiments, trains of 3–15 solitons are created at once [6,8,9,18,19], so that subsequently interactions or collisions between them become relevant. In mean-field theory, these should be akin to collisions of solitons in nonlinear optics, which were well understood earlier [20]. Those results predict effectively attractive interactions for solitons with a mean-field relative phase of $\varphi = 0$ and effectively repulsive interactions for out of phase solitons with $\varphi = \pi$.

Some early doubts were cast on these simple rules by a set of multisoliton experiments (MSE), frequently commencing from explosively heated initial states. These indicated almost exclusively repulsive collisions [6,8,9]. However, a more controlled two-soliton experiment (TSE) shows collisions in apparent agreement with mean-field theory [10,21]. While the MSE results could imply a robust creation of relative π phases between all adjacent solitons [22], the creation of such a pattern cannot be accounted for by theory [23–25]. Rather, studies beyond mean-field theory reported dramatic modifications of soliton interactions by quantum effects [23,26].

Here we extend and consolidate the results of [23,26], by identifying the two essential physical mechanisms that dynamically invalidate mean-field theory. These are first phase diffusion [27] or loss of coherence between colliding solitons and second atom transfer between solitons during a collision, akin to atom tunneling in bosonic Josephon junction (BJJ) [28]. The resultant picture provides more consistency with earlier experimental results than mean-field theory.

We find that phase diffusion must lead to fragmentation of a train of solitons, which consequently exhibits more repulsive collision trajectories than it would otherwise. At zero temperature, the timescale for this fragmentation may be rather long, of the order of seconds. However, we show that fragmentation is significantly accelerated by thermal or uncondensed atoms, and thus can occur on ms timescales for strongly heated condensates.

This article is organized as follows. In Sec. II, we first review soliton collisions in mean-field theory and provide a brief overview of existing experiments on soliton trains and collisions. In Sec. III, we introduce the employed beyond-mean-field techniques. Using these techniques, we then first consider the fragmentation of noninteracting solitons in Sec. IV, and then move to the interplay of fragmentation and soliton collisions in Sec. V. This section separately considers collisions before fragmentation, Sec. V A, after fragmentation, Sec. V B, and the interplay with atom transfer during a collision, Sec. V C; see also Appendix B. We discuss the

*aparna16@iiserb.ac.in
†sebastian@iiserb.ac.in

relevance of broken many-body integrability during collisions in Sec. VI and the dependence on collision velocity in Sec. VII. We then move to a discussion of nonzero temperature and the ramifications of our results in the context of recent experiments in Sec. VIII. Finally, in Sec. IX, we briefly compare the methods employed here, before concluding.

II. MEAN-FIELD SOLITON COLLISIONS

Let us first review soliton collisions in mean field theory. We consider a Bose gas with the second quantized Hamiltonian

$$\hat{H} = \int d^3\mathbf{r}\left\{\hat{\Psi}^\dagger(\mathbf{r})\left[-\frac{\hbar^2}{2m}\nabla^2 + \frac{1}{2}m\omega_\perp^2\mathbf{r}_\perp^2\right]\hat{\Psi}(\mathbf{r}) + \frac{U_{3d}}{2}\hat{\Psi}^\dagger(\mathbf{r})\hat{\Psi}^\dagger(\mathbf{r})\hat{\Psi}(\mathbf{r})\hat{\Psi}(\mathbf{r})\right\}, \tag{1}$$

where the atomic field operator $\hat{\Psi}(\mathbf{r})$ destroys an atom of mass m at location $\mathbf{r}$. The atoms experience 3D s-wave collisions with interaction strength $U_{3d} = 4\pi\hbar^2 a_s/m$, where a_s is the scattering length. The latter is controllable via a Feshbach resonance and assumed to be tuned to attractive interactions $a_s < 0$ to enable bright solitons. Finally atoms are considered free along the direction x, but tightly trapped with trap-frequency $\omega_\perp$ in the transverse directions $\mathbf{r}_\perp = [y,\ z]^T$.

In the simplest mean-field treatment of (1), atomic quantum fluctuations are neglected and the field operator is replaced by the mean-field condensate wave function $\phi(\mathbf{r}) = \langle\hat{\Psi}(\mathbf{r})\rangle$.

We will be exclusively interested in the quasi-one-dimensional (1D) scenario, where the Bose gas is more tightly confined along transverse coordinates $\mathbf{r}_\perp$ than in the longitudinal one x. We then implement the usual 1D reduction, where the 3D mean-field wave function is written as $\phi(\mathbf{r}, t) = \phi(x, t)\eta(\mathbf{r}_\perp)$, with $\eta(\mathbf{r}_\perp) = \exp[-\mathbf{r}_\perp^2/(2\sigma_\perp^2)]/(\sigma_\perp\sqrt{\pi})$, thus assuming transversally the BEC remains in the trap ground state with width $\sigma_\perp = \sqrt{\hbar/(m\omega_\perp)}$, using the transverse oscillator frequency $\omega_\perp$. Then we can derive the quasi-1D Gross-Pitaevskii equation (GPE) for the evolution of the longitudinal mean-field $\phi(x, t)$ using standard methods as

$$i\hbar\frac{\partial}{\partial t}\phi(x,t) = \left[-\frac{\hbar^2}{2m}\frac{\partial^2}{\partial x^2} + U_0|\phi(x,t)|^2\right]\phi(x,t), \tag{2}$$

where $U_0 = U_{3d}/(2\pi\sigma_\perp^2)$ is the effective interaction strength. Importantly, this does not imply that microscopic collisions are constrained to 1D.

For attractive interactions $U_0 < 0$, the GPE (2) has stationary soliton solutions $\phi(x, t) = \phi_{\rm sol}(x)\exp[-i\mu t/\hbar]$ with a spatial profile as sketched in Fig. 1,

$$\phi_{\rm sol}(x) = \mathcal{N}\,\mathrm{sech}(x/\xi), \tag{3}$$

where $\mu = -mN_{\rm sol}^2U_0^2/8/\hbar^2$ is the chemical potential if the soliton contains $N_{\rm sol}$ atoms, ensured by the normalization factor $\mathcal{N} = \sqrt{2|\mu|/U_0}$. The width of the soliton is set by the healing length $\xi = \sqrt{\hbar^2/(2m|\mu|)}$. While the solution (3) is strictly valid for a 1D system only, it aptly describes bright condensate solitons in realistic 3D experiments as long as the transverse trapping $\omega_\perp$ is sufficiently tight [29] and $N_{\rm sol}$ remains safely away from the critical atom number $N_{\rm crit}$ for 3D collapse [8], which we do not discuss here. To study soliton collisions, we now move to a mean-field wave function containing a pair of solitons

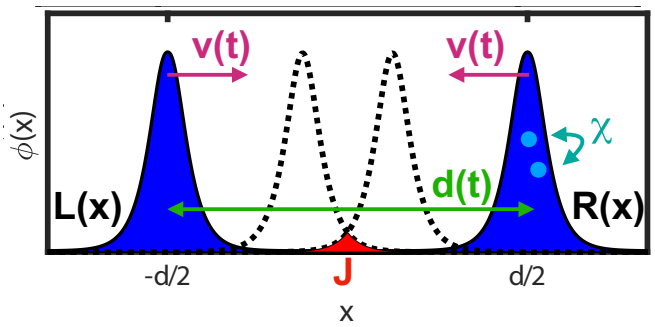

FIG. 1. Sketch of colliding soliton pair with mean-field wave function (4). During the collision, the separation $d(t)$ and velocity $v(t)$ evolve in time. We also sketch two causes for the breakdown of mean-field theory: phase diffusion due to atom-atom interactions within a soliton χ and atom transfer between solitons J, when they are in close proximity.

$$\phi(x,t) = L(x,t)e^{ik(t)x} + e^{i\varphi(t)}R(x,t)e^{-ik(t)x}, \tag{4}$$

with left and right soliton shapes $L(x, t) = \phi_{\rm sol}[x + d(t)/2]$ and $R(x, t) = \phi_{\rm sol}[x - d(t)/2]$. The two solitons are thus separated by a distance d. We also allow a wave number k arising from symmetric soliton motion. The ansatz (4) is sketched in Fig. 1. For a simplified description, we can use a time-dependent variational principle from the Lagrangian based on (1) [20,22] to derive the effective kinetic equations of motion

$$\frac{\partial^2}{\partial t^2}\varphi(t) = 8\,\exp[-d(t)]\sin[\varphi(t)], \tag{5}$$

$$\frac{\partial^2}{\partial t^2}d(t) = -8\,\exp[-d(t)]\cos[\varphi(t)], \tag{6}$$

for the time evolving soliton separation $d(t)$, velocity $v(t) = \hbar k(t)/m$, and relative phase $\varphi(t)$, still based on mean-field theory. We write (5) and (6) for dimensionless variables with $\xi = 1$, $\hbar = 1$, and $m = 1$. Clearly, for $\varphi(t = 0) = 0$ (π), the relative phase does not evolve. We further see that a relative phase $\varphi = 0$ yields attractive and $\varphi = \pi$ repulsive behavior [20,22].

We illustrate in Fig. 2 that the effective kinetic equations (5) and (6) indeed correctly reproduce soliton dynamics predicted by the GPE (2).

Experiments with soliton trains and collisions

While Eq. (6) was largely verified in nonlinear optics relatively soon after its prediction [30], it is still not fully clear to what extent or under which conditions it describes matter-wave solitons.

Soon after the first creation of single matter-wave solitons [5], experiments began to investigate trains or collections of multiple solitons [6,8] that appear when the interactions within a large 1D BEC cloud are suddenly changed from repulsive to attractive using a Feshbach resonance. This led

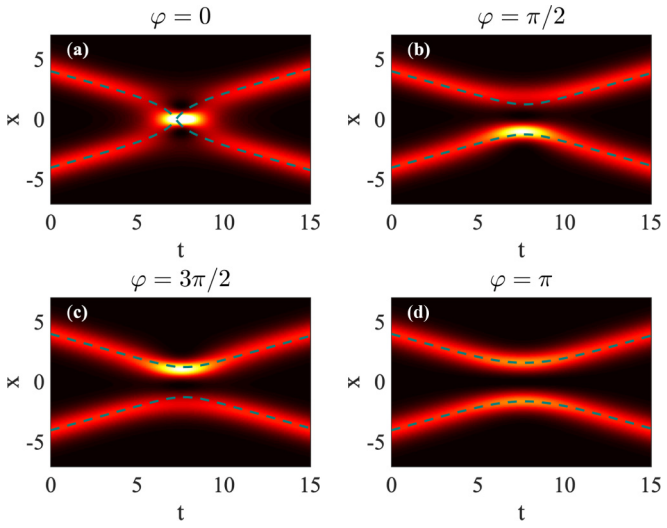

FIG. 2. Review of soliton collisions in mean-field theory for initial relative phase φ of (a) $\varphi = 0$, (b) $\varphi = \pi/2$, (c) $\varphi = 3\pi/2$, and (d) $\varphi = \pi$. The color profile is the atomic density $|\phi(x,t)|^2$ following from (2) for the initial state (4) (black, zero; bright, high). Overlaid dashed teal lines are trajectories based on (6).

to condensate collapse with strong loss of atoms and heating, with remnant atoms forming a train of solitons. Both experiments saw indirect evidence for dominantly repulsive interactions between neighboring solitons in the train: (i) the total remnant atom number after the collapse was still higher than the critical atom number $N_{\rm crit}$ [31] for further collapse, (ii) soliton trajectories, within limited experimental resolution, were typically repulsive, and (iii) almost all solitons survive collisions, which is not the case when interactions are attractive due to further 3D collapse [32,33]. A relative soliton phase of π between neighbors would explain this behavior [4,22,34] as discussed in Sec. II, but such a phase pattern should not actually arise, according to theory [23–25]. A striking counterexample is the repulsively interacting soliton trains with two and four members in [8], for which symmetry requires a phase $\pi = 0$ between the central two solitons.

To address these questions, among others, further experiments were recently performed in the Rice group, tracking soliton collisions using *in situ* observation. In one case, Ref. [10], a condensate was split into two pieces, which were subsequently transformed into solitons in a fairly controlled process, which however took much longer than generating solitons through condensate collapse. We refer to Ref. [10] as the two-soliton experiment (TSE) later. More recently, another soliton train was studied resulting from modulational instability [9], in a multisoliton experiment (MSE). In contrast to earlier MSEs [6,8], a violent initial 3D collapse of the entire cloud into essentially one single high density spike was avoided. The TSE demonstrated that multiple collisions of one soliton pair can be described by the GPE or Eq. (6), *provided that* their relative phase is in fact inferred indirectly from the first of those collisions. The MSE, in turn, again found necessarily repulsive interactions between all neighboring solitons of trains with up to 10 (even) members, since their number remained constant despite the fact that attractive interactions should have resulted in 3D collapse.

It will be important for this article that none of the experiments discussed were in a genuinely 1D regime where one can view also microscopic collisions between atoms as constrained to one dimension. Rather they all fall into the quasi-1D regime, where the BEC system can be reliably mathematically modeled taking into account only one dimension in the trap, but microscopic atomic collisions would still significantly involve three dimensions.

In the following we combine earlier indications of beyond mean-field effects in soliton collisions [23,26] to develop a more comprehensive picture that can reconcile most experimental results above and additionally are suggestive of further quantum dynamical effects, such as entanglement generation, as a subject for future experiments.

III. BEYOND MEAN-FIELD THEORIES

As discussed above, there are experimental and theoretical indications that collisions of bright matter wave solitons may be a case where mean-field theory suffers not only a quantitative but a qualitative breakdown. In this section we now briefly summarize three different beyond mean-field models that can explore this aspect.

A. Two-mode model

One way to go beyond the meanfield expression (4) is with a simple two-mode model (TMM) for the field operator

$$\hat{\Psi}(x) = \overline{L}(x)\hat{a} + \overline{R}(x)\hat{b}, \tag{7}$$

where the left and right "soliton mode functions" $\overline{L}(x) = L(x)/\sqrt{N_{\rm sol}}$ and $\overline{R}(x) = R(x)/\sqrt{N_{\rm sol}}$ are now normalized to one instead of $N_{\rm sol}$ but retain the shape of the soliton. The operator $\hat{a}$ destroys a boson in the left soliton and $\hat{b}$ does the same for the right soliton; they act on Fock states $|\,n,m\,\rangle$, where n (m) is the number of atoms in the left (right) soliton. Thus atomic spatial degrees of freedom are constrained to reside in either the left or right soliton mode. In principle, the TMM can straightforwardly be extended to describe the problem in three spatial dimensions, by augmenting to modes $\overline{L}(\mathbf{x})$, $\overline{R}(\mathbf{x})$ to 3D functions, assuming the same simplified transverse shape as discussed in Sec. II.

We now allow number fluctuations and, through these, varying phase relations. In a Fock state $|\,n,m\,\rangle$ the relative phase between solitons is undefined, while in a two-mode coherent state

$$|\alpha,\beta\rangle = |\alpha\rangle \otimes |\beta\rangle, \tag{8}$$

with $|\alpha\rangle = e^{-\frac{|\alpha|^2}{2}} \sum_{n=0}^{\infty} \frac{\alpha^n}{\sqrt{n!}}|n\rangle$, the relative phase is $\varphi = \arg[\alpha] - \arg[\beta]$. This two-mode coherent state has an uncertain total atom number.

Even for fixed total atom number $N_{\rm tot}$ we can assign a well-defined relative phase between left and right soliton, using a relative coherent state in the even or odd soliton pair $|N_{\rm tot},\pm\rangle \equiv [(\hat{a} \pm \hat{b})/\sqrt{2}]^{N_{\rm tot}}/\sqrt{N_{\rm tot}!}|0\rangle$.

Inserting (7) into (1), assuming *real* mode functions with a narrow Gaussian shape along transverse directions, we obtain

the TMM Hamiltonian

$$\hat{H} = \omega(\hat{a}^\dagger\hat{a} + \hat{b}^\dagger\hat{b}) + \frac{\chi}{2}(\hat{a}^\dagger\hat{a}^\dagger\hat{a}\hat{a} + \hat{b}^\dagger\hat{b}^\dagger\hat{b}\hat{b}) + J(\hat{b}^\dagger\hat{a} + \hat{a}^\dagger\hat{b}) + \bar{U}(4\hat{a}^\dagger\hat{a}\hat{b}^\dagger\hat{b} + \hat{a}^\dagger\hat{a}^\dagger\hat{b}\hat{b} + \hat{b}^\dagger\hat{b}^\dagger\hat{a}\hat{a}) + 2\bar{J}(\hat{a}^\dagger\hat{a} + \hat{b}^\dagger\hat{b} - 1)(\hat{b}^\dagger\hat{a} + \hat{a}^\dagger\hat{b}), \tag{9}$$

with coefficients

$$\omega = \int dx\, \bar{L}(x)\left[-\frac{\hbar^2}{2m}\frac{\partial^2}{\partial x^2}\right]\bar{L}(x), \tag{10a}$$

$$\chi = U_0 \int dx\, \bar{L}(x)^4 = -\frac{mU_0^2 N_{\rm sol}}{6\hbar^3}, \tag{10b}$$

$$J(d) = \int dx\, \bar{L}(x)\left[-\frac{\hbar^2}{2m}\frac{\partial^2}{\partial x^2}\right]\bar{R}(x), \tag{10c}$$

$$\bar{U}(d) = \frac{U_0}{2}\int dx\, \bar{L}(x)^2\bar{R}(x)^2, \tag{10d}$$

$$\bar{J}(d) = \frac{U_0}{2}\int dx\, \bar{L}(x)^3\bar{R}(x). \tag{10e}$$

We indicated with an argument d whether a coefficient depends on the distance between the left and right soliton modes. The TMM will be useful in Sec. IV to elucidate the basic physics underlying the predictions of the more involved quantum many-body theories discussed further below.

For large d, when $J, \bar{U}, \bar{J} \to 0$, the TMM can be analytically solved, as shown in Sec. IV. In the more general case, we will numerically solve the time-dependent Schrödinger equation for $|\,\Psi(t)\,\rangle$, *coupled* to Eq. (6) via $d(t)$. The coefficients J, $\bar{U}$, and $\bar{J}$ in Eq. (9) then vary in time, due to their dependence on the soliton separation $d(t)$. We used $|\,\alpha, \beta\,\rangle$ as initial state when comparing with TWA (see Sec. III C) and $|\,N_{\rm tot}, \pm\,\rangle$ for comparisons with MCTDHB (see Sec. III B).

B. Multiconfigurational time-dependent Hartree for bosons (MCTDHB)

The TMM is made more sophisticated in MCTDHB [35] with two orbitals. In essence the latter allows a combination of the mean-field and the two-mode approach. It allows the bosons to condense into two orbitals, as the quantum field operator is again expanded as

$$\hat{\Psi}(x,t) = \phi_+(x,t)\hat{c}(t) + \phi_-(x,t)\hat{d}(t). \tag{11}$$

This includes the ansatz (7) but importantly now contains two orbitals $\phi_\pm(x,t)$ that can self-consistently evolve in time. Their evolution and that of the Fock states onto which $\hat{c}$, $\hat{d}$ act is determined from a time-dependent many-body variational principle [35]. In contrast, in the TMM, the time dependence of L, R is fixed *a priori*.

Initially, the orbitals are taken as the symmetric or antisymmetric linear combination of the soliton modes $\phi_\pm(x,t) = [\bar{L}(x) \pm \bar{R}(x)]/\sqrt{2}$. Depending on the initial relative phase φ between the solitons, either is initially fully occupied. Since MCTDHB operates with a fixed total atom number, the corresponding initial state in the two-mode model is $|\,N_{\rm tot}, \pm\,\rangle$.

We refer to the original article [35] for the equations of motion and the extensive literature for details. The method has proven particularly useful to study scenarios involving dynamical condensate fragmentation [36–40], scenarios generating entanglement [41–44], and few-body dynamics [45]. Here we use the open-MCTDHB package [46].

Important approximations contained in the ansatz (11) are the reduction from three spatial dimensions to one, with the same argumentation as in Sec. II, and the reduction of the many-mode quantum field problem to the substantially simplified two-mode constraint.

C. Truncated Wigner approximation (TWA)

We finally drop the two-mode constraint, moving to an (approximate) multimode quantum field theory. An effective approximation technique for those is the truncated Wigner framework [47–50], where the quantum many-body state is represented by an ensemble of stochastic trajectories. In TWA we solve the same equation of motion as for mean-field theory (2), albeit with random noise added to the initial state

$$\phi(x,0) = \phi_0(x) + \sum_\ell \frac{\eta_\ell u_\ell(x)}{\sqrt{2\,\tanh\left(\frac{\epsilon_\ell}{2k_BT}\right)}}, \tag{12}$$

with $\phi_0(x)$ the mean-field soliton pair (4). The index ℓ numbers a plane-wave basis $u_\ell(x) = e^{ik_\ell x}/\sqrt{\mathcal{V}}$ with normalization volume $\mathcal{V}$; then $\epsilon_\ell = \hbar^2 k_\ell^2/(2m)$. The η_ℓ are complex Gaussian noises with unit variance and correlations $\overline{\eta_\ell\eta_j} = 0$, $\overline{\eta_\ell^*\eta_j} = \delta_{\ell j}$ and T is the system temperature. Overlines indicate stochastic averages. The TWA described here is known to give good results for decoherence phenomena [51,52] as long as the noise amplitude added is dominated by the mean field [53–56], but it would usually fail to capture, e.g., quantum revivals [51,52] such as those exhibited by the model (9) at later times.

Quantum correlations are extracted according to

$$\langle\hat{\Psi}^\dagger(x')\hat{\Psi}(x)\rangle = \overline{\phi^*(x')\phi(x)} - \tfrac{1}{2}\delta_c(x,x'), \tag{13}$$

where $\delta_c(x,x') = \sum_\ell u_\ell(x)u_\ell^*(x')$ is a restricted basis commutator [56]. Our TWA calculations and TMM solutions employ the XMDS package [57,58]. We will later use TWA for comparison with MCTDHB, simulation of experiments and for the incorporation of finite temperature.

The truncated Wigner method derives its name from the truncation of the evolution equation for the distribution function of stochastic trajectories, in order to bring that into the form of a Fokker-Planck equation [47]. This approximation is motivated by practicalities and its physical implications often far from obvious. Later work has, however, shown that the approximation will be good for short times (where it is again not *a priori* obvious how short) [53] and as long as most modes of the quantum field are highly occupied [48,49]. In practice this means that the noise amplitude added in (12) ought to be small compared to the mean-field amplitude $|\phi_0(x)|$ [54–56].

D. Coherence and fragmentation

Within all three many-body models, we are mainly interested in the resultant coherence and fragmentation dynamics. To identify the condensate in a quantum-field setting, we use the Penrose-Onsager criterion [1,59,60], that the largest eigenvalue of the one-body density matrix (OBDM) is the

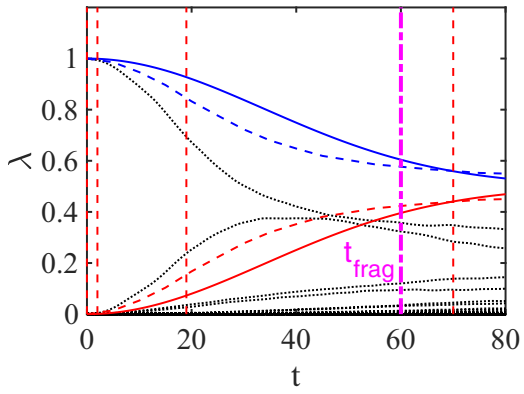

FIG. 3. Fragmentation of far separated BEC solitons. We show the relative occupation λ of all system orbitals at zero temperature in TWA (black dotted), MCTDHB (blue and red dashed), and two-mode model (blue and red solid). For MCTDHB and two-mode model there are only two orbitals by construction, for TWA two dominate. Initially we have a pure BEC of two solitons since $\lambda = 1$ for one orbital. It then fragments around $t_{\rm frag}$ as defined in the text, indicated by the vertical magenta dot-dashed line. The nonlinear parameter, see Eq. (10b), is $\chi = -6.6 \times 10^{-4}$. Vertical red-dashed lines are the times for which we plot snapshots of the Q function in Fig. 4.

condensate occupation, with OBDM

$$\varrho(x, x') = \langle \hat{\Psi}^\dagger(x')\hat{\Psi}(x)\rangle. \tag{14}$$

The eigenvalues λ_j are then obtained from $\int dx' \varrho(x, x')\chi_j(x') = N\lambda_j\chi_j(x')$, where $\chi_j(x)$ is the corresponding single particle orbital and $N = 2N_{\rm sol}$. If two λ_j are of order unity, the system is called *fragmented* [1]. In the TWA the OBDM is given by (13), and in MCTDHB by $\varrho(x, x') = \sum_{kq}\langle \hat{O}_k^\dagger \hat{O}_q\rangle \phi_k^*(x', t)\phi_q(x, t)$ [61], using $k, q \in \{+, -\}$ and $\hat{O}_+ = \hat{c}$, $\hat{O}_- = \hat{d}$; see (11).

For the TMM, we can ignore the frozen spatial structure and focus on the mode space OBDM

$$\varrho = \begin{bmatrix} \langle \hat{a}^\dagger \hat{a}\rangle & \langle \hat{b}^\dagger \hat{a}\rangle \\ \langle \hat{a}^\dagger \hat{b}\rangle & \langle \hat{b}^\dagger \hat{b}\rangle \end{bmatrix}. \tag{15}$$

We denote the two eigenvalues of ϱ with λ_+ (the larger one) and λ_- (the smaller ones), in the following.

IV. SOLITON PAIR FRAGMENTATION DUE TO PHASE DIFFUSION

We now initially consider the beyond mean-field evolution of two solitons far separated from each other so that they can be considered noninteracting. They are initialized as part of one coherent, nonfragmented BEC. We show in Fig. 3 the eigenvalues of the OBDM predicted by all three methods discussed above.

By the indicated time, $t_{\rm frag}$, the eigenvalues λ_+ and λ_- have clearly become comparable and the system is thus fragmented. We formally call the system fragmented after $t_{\rm frag}$, when $|\lambda_+(t_{\rm frag}) - \lambda_-(t_{\rm frag})| \equiv \Delta\lambda = 0.2$. The choice of $\Delta\lambda$ is somewhat arbitrary. We cannot chose $\Delta\lambda = 0$, since we later show cases where the $\lambda_\pm$ are never quite equal, yet get very close and should still indicate fragmentation.

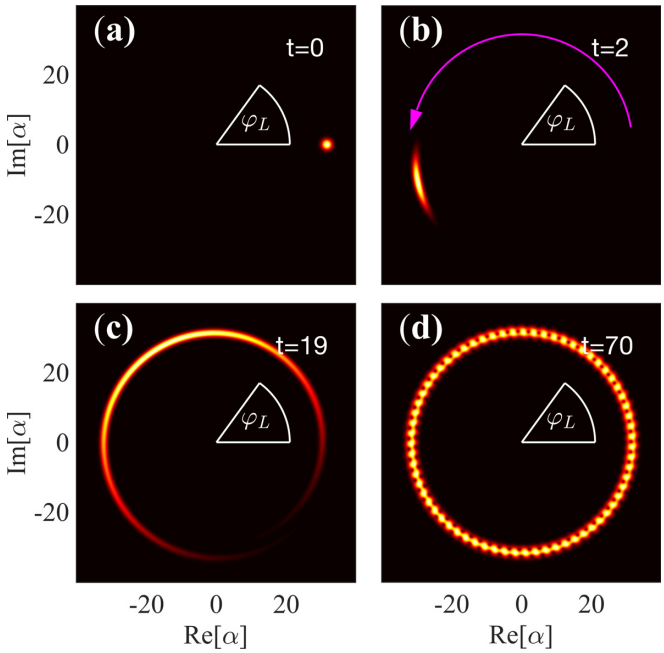

FIG. 4. Phase diffusion for the same case as in Fig. 3, at times indicated there as red-dashed vertical lines. We plot the Husimi Q function $Q(\alpha)$ of a single soliton's internal state [62]; see text. (black, zero; bright, high) (a) Initially, $t = 0$, this corresponds to a coherent state. For later times as indicated in (b), (c), and (d), the Q function shows shearing (Kerr squeezing) and eventually indicates a completely undefined soliton phase φ_L.

All three methods agree on the fragmentation timescale defined above. Quantitative differences are expected, due to the varying numbers of modes and constraints on these among the methods. The origin of fragmentation is best understood in the TMM. The coefficients J, $\bar{U}$, and $\bar{J}$ in (9) depend on the overlap of $\bar{L}(x)$ and $\bar{R}(x)$ and thus on d. For large soliton separations d, all these vanish, and only the first line in (9) remains. The dynamics can then be determined analytically

$$|\,\Psi(t)\,\rangle = \sum_{nm} c_{nm}(t)|\,nm\,\rangle,$$
$$c_{nm}(t) = c_{nm}(0)e^{-i\{E_0(n+m)+\frac{\chi}{2}[n(n-1)+m(m-1)]\}t/\hbar}, \tag{16}$$

where the coefficients $c_{nm}(0)$ are set by the two-mode coherent initial state (8) with amplitude α, $\beta = \sqrt{N_{\rm sol}}$. From (16) we obtain the eigenvalues of (15) as

$$\lambda_\pm = \frac{1 \pm e^{2N_{\rm sol}[\cos(\chi t/\hbar)-1]}}{2} \approx \frac{1 \pm e^{-(t/t_{\rm frag})^2}}{2}, \tag{17}$$

where the expression after $\approx$ is valid for short times. The fragmentation timescale $t_{\rm frag} = \hbar/(\sqrt{N_{\rm sol}}|\chi|)$ is corroborated by the more involved quantum many-body methods TWA and MCTDHB in Fig. 3. For the TWA results in Fig. 3, we can see the emergence of several additional significantly occupied orbitals beyond the first two.

Note that the Hamiltonian (9) for large d reduces to $\hat{H} = \frac{\chi}{2}(\hat{a}^\dagger\hat{a}^\dagger\hat{a}\hat{a} + \hat{b}^\dagger\hat{b}^\dagger\hat{b}\hat{b})$, after we adjust the zero of energy such that the term $\sim\omega$ can be ignored. This just corresponds to two independent nonlinear Kerr oscillators and the dynamics just discussed thus is well known and referred to as Kerr squeezing

[62–64] or phase diffusion [27]. Phase diffusion refers to an initially fixed condensate mean phase becoming ill defined due to diffusion over all angles.

We visualize phase diffusion for the reduced state of just one (the left) soliton in Fig. 4, using the Husimi Q function $Q(\alpha) = |\langle \alpha \,|\, \Psi \rangle|/\pi$ that quantifies the overlap of an arbitrary state $|\,\Psi(t)\,\rangle$ with a coherent state $|\,\alpha\,\rangle$. In the space $\alpha \in \mathbb{C}$, farther from the origin corresponds to larger atom number n in the left soliton, and the argument of α indicates the soliton phase φ_L. We show $Q(\alpha)$ at several characteristic snapshots, indicated in Fig. 3 by vertical red dashed lines. Initially, the state of atom number within one of the solitons itself is a coherent state, with a 2D Gaussian as Q function. It then shears, since the angular phase evolution due to nonlinear interactions scales as $\varphi_L \sim \chi n(n-1)t$ with the atom number, and is thus faster for α farther away from the origin. During this initial period, see, e.g., $t = 2$, the dynamics is also called Kerr squeezing. At later times, the phase of a single soliton becomes progressively undefined. Hence the relative phase between two solitons will be even less well defined. At that stage, there also is complete fragmentation.

Phase diffusion in the context of BEC solitons was explored before [65,66]. It has been linked to fragmentation in the context of soliton interferometry [67]. Here we clearly identify it as the root physical cause of soliton train fragmentation, first reported in [26]. Most importantly, this enables us to make analytic predictions for the fragmentation timescale $t_{\rm frag}$ in (17) and will in the future allow assessments of how fragmentation would depend on the number statistics of the initial state.

V. SOLITON COLLISIONS

We now consider the effect of the fragmentation discussed above on the collisions of condensate solitons. We want to distinguish two cases: collisions occurring before fragmentation and after fragmentation. To this end, initially unfragmented solitons separated by a distance $d_{\rm ini}$ are given an initial velocity $v_{\rm ini}$ towards each other such that their expected collision time is approximately $t_{\rm coll} = |d_{\rm ini}/(2v_{\rm ini})|$. We show in Figs. 5 and 6 the atom density in a colliding soliton pair from MCTDHB (Sec. III B) as color shade, compared with the collision trajectory based on the kinetic equation (6) as overlayed dashed teal line. Since (6) is based on the GPE (2), we are thus directly comparing mean field with beyond-mean-field collisions.

In both figures, the collision velocity is adjusted to $v_{\rm ini} = 0.2$. We then employ $d_{\rm ini} = 8$ in Fig. 5, yielding an expected collision time $t_{\rm coll} = 20$, which is *before* the expected fragmentation time of $t_{\rm frag} = 60$ for far separated solitons, based on Eq. (17). In contrast, for Fig. 6, $d_{\rm ini}$ is changed to $d_{\rm ini} = 32$; hence $t_{\rm coll} = 80$ becomes larger than $t_{\rm frag}$.

A. Before fragmentation

Let us consider collisions before fragmentation first. We see in Figs. 5(a) and 5(c) that quantum many-body theory and mean-field theory agree on the character of collisions in this case. Most notably the initial relative phase controls whether interactions are attractive or repulsive. Note that the color

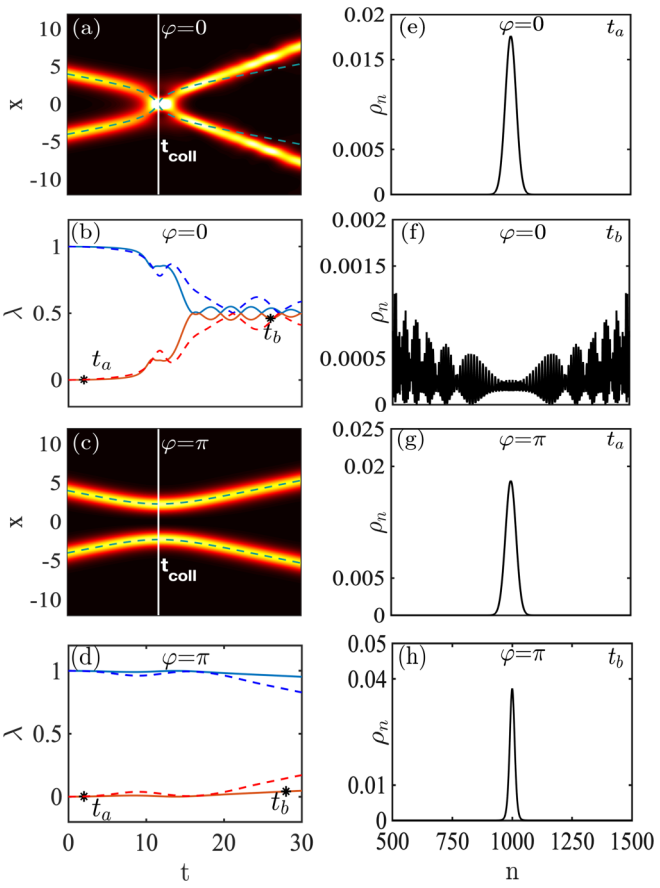

FIG. 5. Collision and coherence dynamics in controlled soliton collisions *before* fragmentation, $t_{\rm coll} < t_{\rm frag}$. The initial relative phases between solitons, φ, are indicated. (a),(c) Total atomic density (black, zero; bright, high) from MCTDHB and expected mean-field trajectories based on Eqs. (2) and (6) (dashed teal line). (b),(d) The two largest orbital populations $\lambda(t)$ from MCTDHB (dashed) and the two mode model (7) (solid). For the latter we used a time-dependent soliton separation $d(t)$, which is inferred from the MCTDH peak densities. (e),(g) Precollision atom number probabilities ρ_n in the left soliton from the TMM at the times t_a indicated by ($\star$) in (b),(d); the total number is fixed at 2000, with on average 1000 in each soliton. (f),(h) The same after the collision, at times t_b in (b),(d). The figure uses dimensionless units as discussed in Appendix A.

shading indicates the total or mean atomic density from MCTDHB, which contains contributions from all orbitals present in (11) and depends on the quantum state. Collisions actually occur slightly earlier than the estimate $t_{\rm coll} = |d_{\rm ini}/(2v_{\rm ini})|$, due to the finite range of intersoliton interactions. The post-collision deviations of the trajectories visible in panel (a) are commented upon in Sec. V C.

In addition to the atom density and hence trajectories, MCTDHB also provides us with the time evolution of the eigenvalues of the OBDM $\lambda_\pm$, shown in panels (b) and (d). We compare these with the $\lambda_\pm$ obtained from the TMM discussed in Sec. III A, with trajectories $d(t)$ adjusted to those in MCTDHB. It is apparent that collisions indeed occur prior to fragmentation and the two models yield similar OBDM eigenvalues. The TMM now additionally allows us to inspect the atom number distribution in the left soliton $\rho_n = \sum_m |c_{nm}|^2$; see Sec. IV.

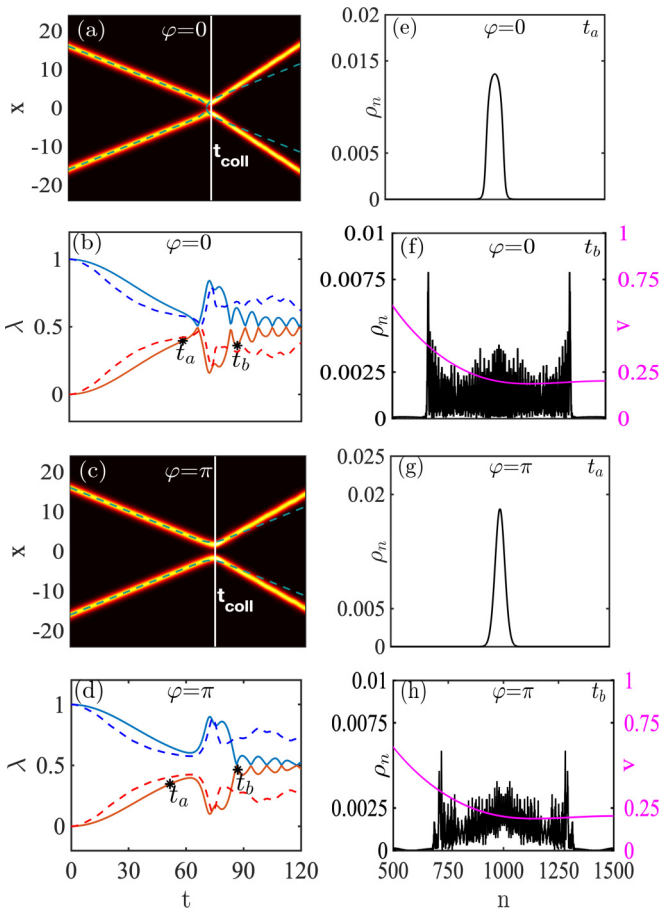

FIG. 6. Collision and coherence dynamics in controlled soliton collisions *after* fragmentation, $t_{\rm coll} > t_{\rm frag}$. Panel layout and curves as in Fig. 5. Magenta lines and axes in panels (f),(h) additionally show the dependence of postcollision velocity $v = p_+/m$ on atom number per soliton; see Sec. V D and Appendix B.

We show this distribution in Figs. 5(e)–5(h) at the times indicated by (⋆) in panels (b) and (d), which are chosen just before and just after the collision. Outside of the time window $[t_a, t_b]$, the number distribution is essentially conserved. The early snapshots at t_a in panels (e) and (g) thus approximately show the Gaussian ρ_n for the initial relative coherent state $|N_{\rm tot}, \pm\rangle$. However, during closest approach, near $t_{\rm coll}$ atom transfer terms containing the operator $\hat{b}^\dagger\hat{a} + \hat{a}^\dagger\hat{b}$ become large in (9) (terms $\sim J, \bar{J}$). Atoms can thus make transfers from one soliton to the other. This intermittent bosonic Josephson junction (BJJ) [28] causes a widening of the number distribution for the initial phase $\varphi = 0$; see panel (f). This wider number distribution then accelerates the phase diffusion effect discussed in Sec. IV and causes subsequent fragmentation already around $t_{\rm frag} = 15$, where without the collisions it would have only happened at $t_{\rm frag} \approx 60$. Note, however, that the TMM results for the $\varphi = 0$ may not be reliable, since exactly at the moment of collision the two chosen modes cease to be orthogonal. However, this is not a problem shared by MCTDH, which qualitatively agrees on an increase of the degree of fragmentation following the collision, albeit less severe. We thus conclude that attractive collisions will cause earlier subsequent fragmentation.

In contrast, the number distribution is not significantly widened in the repulsively interacting case in panel (h), due to much weaker tunneling. Note that this is not alone due to the minimal separation being larger in the repulsive case than in the attractive case: interaction terms become almost as large as in the $\varphi = 0$ case anyway. Thus the $\varphi = \pi$ phase relation must be less conducive to atom transfer.

B. After fragmentation

We now move to collisions after fragmentation, $t_{\rm coll} > t_{\rm frag}$. In that case almost no initial phase dependence of collision kinematics remains in the mean atomic density provided by MCTDHB; see Figs. 6(a) and 6(c). Mean collision trajectories always seem to have repulsive character, fairly regardless of the *initial* relative phase between the solitons. It has been shown in [68], however, that an "always repulsive" appearance of the MCTDHB total atomic density may be misleading. The authors of Ref. [68] include all available information on the many-body wave function to predict the atom density for single realizations of the many-atom probability distribution for fragmented collisions, instead of the mean density that one would obtain by averaging many such realizations. Following these many-body collisions in time, one identifies collision trajectories akin to mean-field ones, with seemingly random phases from realization to realization, including some attractive collisions.

We see the same behavior in TWA collisions from a fully fragmented state. Also there, single trajectories are a random mix, exhibiting collisions that match the mean-field picture for all relative phase angles $\varphi \in [0, 2\pi)$ between solitons. A majority of these collisions have a repulsive "appearance"; thus a density average over all such trajectories yields a repulsive mean trajectory. Features of both simulation techniques are consistent with the picture in Sec. IV: after complete phase diffusion, all relative phases between the two solitons are part of the two soliton quantum state, so an individual collision may appear repulsive with some probability and with another attractive.

C. Collisions with number change

Besides the apparent indifference of mean collisions to the initial intersoliton phase, a second prominent feature of Fig. 6 is that MCTDHB predicts collisions to be *superelastic*, with solitons gaining kinetic energy in the collision, while total energy is conserved. This feature was also visible in panel (a) of Fig. 5. To understand possible physical reasons for this, we first multiplied the right-hand side (RHS) of the soliton kinetic equation (6) used for the TMM with a scale factor $f(t)$, phenomenologically adjusted to give trajectories in agreement with MCTDHB, i.e., speeding up in the collision. We can then get a first idea of the source of additional kinetic energy by inspecting the different contributions to the total energy

$$E_{\rm tot} = \langle \hat{H} \rangle + E_{\rm kin}, \tag{18}$$

within the corresponding TMM in Fig. 7.

We can obtain $\langle \hat{H} \rangle$ from (9), while the joint kinetic energy of both solitons, each with velocity $\dot{d}(t)/2$, is

$$E_{\rm kin} = 2 \times \frac{1}{2} m N_{\rm sol} \left(\frac{\dot{d}(t)}{2} \right)^2. \tag{19}$$

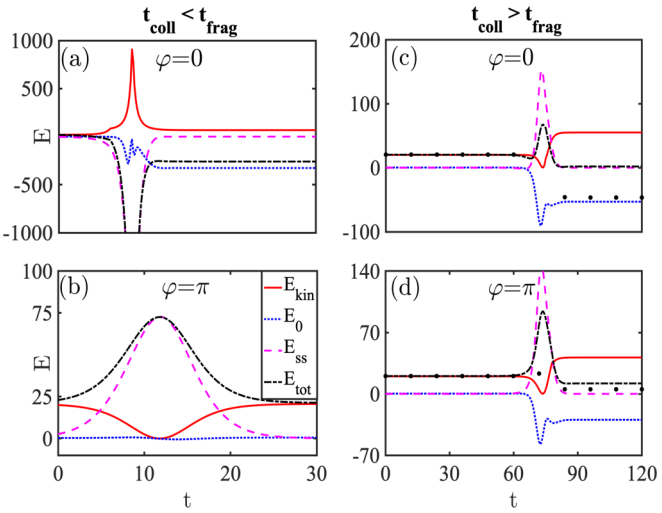

FIG. 7. Conversion of mean interaction energy into kinetic energy during a soliton collision, using TMM with soliton distance $d(t)$ taken from MCTDHB. We show the total energy $E_{\rm tot}$, Eq. (18) (black dot-dashed), the kinetic energy, Eq. (19) (solid red) $E_{\rm kin}$, the soliton self-interaction energy (dotted blue) E_0, Eq. (20), and inter-soliton interaction energy (dashed magenta) $E_{\rm ss}$, defined in the text. (a),(b) Collision before fragmentation with (a) $\varphi = 0$ and (b) $\varphi = \pi$. (c),(d) Collision after fragmentation with (c) $\varphi = 0$ and (d) $\varphi = \pi$. In (c),(d), black (•) show $E_{\rm tot}$ if we do not include an increase in kinetic energy.

We then further split $\langle \hat{H} \rangle$ into a contribution internal to the solitons

$$E_0 = \langle \omega(\hat{a}^\dagger \hat{a} + \hat{b}^\dagger \hat{b}) + \frac{\chi}{2}(\hat{a}^\dagger \hat{a}^\dagger \hat{a}\hat{a} + \hat{b}^\dagger \hat{b}^\dagger \hat{b}\hat{b}) \rangle \tag{20}$$

and a soliton-soliton interaction energy $E_{\rm ss}$ [all other terms of (9)]. For large separations $d(t)$, we must have $E_{\rm ss} \to 0$.

We plot all energy contributions in Fig. 7, setting the initial value of E_0 to zero, to ease the comparison of temporal changes. We see in panels (c) and (d) of Fig. 7 that the drop in internal soliton energy, E_0, provides the extra kinetic energy found after collisions. We identify the atomic transfer between the solitons discussed earlier as cause for this, due to interactions of the form $\hat{J}(d)(\hat{b}^\dagger \hat{a} + \hat{a}^\dagger \hat{b})$. Here the coefficient $\hat{J}(d)$ depends on the overlap of the left and right soliton modes, and is relevant only briefly around the moment of collision. As shown in Figs. 6(b) and 6(d), the term causes significant restoration of phase coherence, with an accompanying widening of the atom number distribution ρ_n in each soliton, Figs. 6(f) and 6(h). This is in accordance with number and phase being conjugate variables.

Since the internal energy per soliton $E_0 \approx \chi \sum_n \rho_n n^2$ is negative and nonlinearly dependent on atom number, an increase of the atom number uncertainty and thus widening of the distribution ρ_n causes an internal energy drop $\Delta E_0 \approx \chi \sum_n \Delta\rho_n n^2$, where $\Delta\rho_n$ is the difference between the number distributions before and after the collision. We find that this can quantitatively explain the gain in kinetic energy as shown in Figs. 7(c) and 7(d), up to a minor mismatch.

This minor mismatch is not surprising since we combine information from two independent methods (MCTDHB and TMM) that are not expected to be consistent in this combination. The point we stress is that if solitons gain kinetic energy, the drop in internal energy is partially balanced in contrast to elastically colliding solitons, as seen by comparing black lines and black dots in Figs. 7(c) and 7(d). The explanation works less well for panel (a). However, in that case the TMM is expected to break down at the moment of the collision, since the two modes become identical in that effectively attractive case.

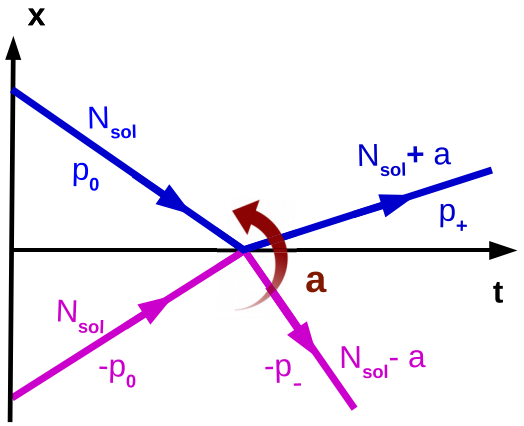

FIG. 8. Momenta involved in a collision with exchange of atoms. The incoming solitons on the left of the graph contain $N_{\rm sol}$ atoms, with momentum $\pm p_0$, respectively. If a atoms transfer from one soliton to the other, the larger one must move slower after the collision to conserve the total momentum. This is the case in a single realization of the quantum many-body superposition state.

D. Momentum balance in collisions with number change

However, now that we have linked the increase in postcollision mean kinetic energy of solitons with atoms transferring from one soliton to the other, we must consider the implications of this picture, when taking into account momentum conservation. To this end we refer to Fig. 8. For simplicity of the following argument, assume an equal number of atoms, $N_{\rm sol}$, are contained in the two incoming solitons with momenta p_0 and $-p_0$ per atom sketched in Fig. 8; thus the initial total net momentum is zero.

At the moment of collision, due to close proximity of solitons, atom transfer from one to the other is likely. Let us assume a atoms are transferred from the left to the right soliton. If we denote the outgoing momenta per atom by p_+ and $-p_-$, conservation of momentum gives

$$(N_{\rm sol} + a)p_+ - (N_{\rm sol} - a)p_- = 0, \tag{21}$$

which for $a > 0$ already clearly requires $|p_-| > |p_+|$ as sketched in the figure.

An additional constraint arises from energy conservation

$$N_{\rm sol}\frac{p_0^2}{m} + \chi N_{\rm sol}^2 = (N_{\rm sol} + a)\frac{p_+^2}{2m} + \chi\frac{(N_{\rm sol} + a)^2}{2} + (N_{\rm sol} - a)\frac{p_-^2}{2m} + \chi\frac{(N_{\rm sol} - a)^2}{2}. \tag{22}$$

Equations (21) and (22) can be solved to yield momenta of atoms in outgoing solitons $p_\pm$ as a function of their initial constituent number $N_{\rm sol}$, the number of atoms transferred in

the collision a, initial momentum per atom p_0, and Hamiltonian parameters m, χ. We find

$$|p_+| = \frac{\sqrt{a - N_{\rm sol}}\sqrt{a^2 m\chi - p_0^2 N_{\rm sol}}}{\sqrt{aN_{\rm sol} + N_{\rm sol}^2}}. \tag{23}$$

The resultant velocity $v(n) = p_+/m$ as a function of soliton constituent number $n = N_{\rm sol} + a$ is shown as magenta lines in Figs. 6(f) and 6(h).

Importantly, $v(n)$ is not symmetric about $N_{\rm sol}$ and *nonlinear*, such that if we calculate the mean outgoing kinetic energy $\bar{E}_{\rm kin}$ as the average of kinetic energies $E_{\rm kin}[v(n)] = mv(n)^2/2$ over the distribution of atom numbers in the soliton $\bar{E}_{\rm kin} = \sum_n \rho_n E_{\rm kin}[v(n)]$, the result can be *larger* than the ingoing kinetic energy and agrees quite closely with the MCTDHB proposal. On average, we can view this kinetic-energy gain as fueled by a drop in the internal soliton energy due to a widening of ρ_n. Of course, note that the average atom transfer $\bar{a}$ must be zero by symmetry; thus if transfer of a atoms occurs with some probability, the same is true for $-a$.

In the discussion of Sec. V D so far, we have neglected the initial atom number unncertainty required to implement a defined intersoliton phase. Based on Figs. 6(e)–6(h), these are small compared to fluctuations generated through atom transfer.

We thus propose the following: in the superelastic cases, the MCTDHB method provides a variationally optimized approximation within its two-mode constraint, to describe an entangling quantum many-body collision beyond its reach: according to the arguments above, we would conclude that the postcollision soliton state for the two solitons is mesoscopically entangled, with a superposition of solitons of different constituent numbers located at different *positions*, since they have moved with different velocities. Schematically we can write this state as

$$|\Psi_{\rm pc}\rangle = \sum_{n_s} c_{n_s} |n_s, v(n_s)\rangle_L \otimes |2N_{\rm sol} - n_s, v(2N_{\rm sol} - n_s)\rangle_R, \tag{24}$$

where $|n, v\rangle$ indicate the constituent number n and velocity v (hence also position) of the left and right soliton separately and c_{n_s} are complex coefficients.

Of course, this also implies that the TMM and MCTDHB, which have provided this picture, cannot be valid for times much after the collision since their restriction to a single spatial mode or orbital per soliton precludes the description of an entangled state of position such as (24). For that one orbital per soliton and per contributing velocity class would be required. However, the two physical causes of this final state, phase diffusion before collisions and atom transfer at the moment of collision, both occur during the time in which the models are expected to be valid for the effectively repulsive collisions. We thus expect our conclusions to persist qualitatively, unless some essential conservation law was broken by the approximations in the methods discussed in Sec. III. One such conservation law would be provided by microscopic momentum conservation in a strictly 1D setting, but not in 3D as discussed in the next section.

The state (24) is motivated by the processes discussed with evidence provided by the effective models used here. Once allowing significant non-mean-field effects, other possibilities that those models could not have hinted at are for example the emission of atoms as radiation from the solitons [69].

The schematic (24) constitutes the many-body generalization of semiclassical results [70] and is also reminiscent of the collision induced two species Bell states proposed in [71] and entanglement generation involving dark [72] or dark-bright solitons [44].

VI. INTEGRABILITY BREAKING

Let us now discuss the connection of the previous section with the absence of many-body integrability of the underlying model. In a more extremely 1D scenario, where *individual atomic collisions* can also be restricted to the single dimension x, a 1D variant of the Hamiltonian (1) would become that of the Lieb-Liniger-McGuire (LL) model [73,74]. This model is integrable with an exact many-body solution, which contains the feature that the set of *individual* atomic momenta is conserved [73,75,76]. Intuitively, in a setting such as Fig. 8, the atoms within a soliton copropagate in the incoming state, all with individual momenta either p_0, if they are in the left soliton, or $-p_0$ if they are in the right one. The binary delta function interaction potential $\delta(x_1 - x_2)$ between atoms 1 and 2 then can change the momentum of the atom pair only as in $(p_0, -p_0) \to (-p_0, p_0)$, i.e., a completely elastic momentum flip collision. This would preclude atom transfer processes as described in Sec. V D, since the momenta would always remain distributed at $N/2$ atoms with p_0 and $N/2$ atoms with $-p_0$.

While this *collisionally* 1D regime has attracted considerable experimental attention [77–79], it is not at all reached in any of the soliton experiments discussed in this article; see Sec. II. There, atoms are much more weakly confined transversely and collisions are thus 3D, significantly breaking integrability [80]. Also the presence of a harmonic trap in the longitudinal direction contributes to integrability breaking [75]. In such a scenario, methods in which many-body integrability is implicitly broken, which applies to all those presented in our Sec. III, will provide *qualitatively more physical* results than an artificially integrable method would. For example, consider the free expansion of a repulsively interacting quasi-1D condensate in a wave guide as in the experiment [81]: here the initial interaction energy is converted into kinetic energy by collisions, causing the momentum distribution to widen dynamically. This effect is not captured by the LL model, but is *quantitatively* captured by the quasi-1D GPE (2). In the same sense we believe our methods paint a more physical picture of quasi-1D solitary wave collisions than the LL model would, which indeed does not contain atom transfer [66]. Other work dealing with broken integrability in the context of soliton collisions also reported signs of atom transfer [75,82].

The connection of atom exchange during soliton collisions and (non)integrability warrants further studies. Experiments could vary the degree of transverse confinement to enforce a transition between the regimes, while theory can explicitly introduce integrability breaking terms as in [75] or [80] to the models discussed here. Besides these possibilities, the solitary

wave collision scenario represents a surprisingly daunting scenario for theory: it would be desirable to employ a full fledged first-principles simulation that would have to deal with three spatial dimensions, mesoscopic entanglement, and thermal noise (see Sec. VIII) all at once. We are not aware of a formalism that is capable of all these at present. Nonetheless, we have confidence in our conclusions, since they are based on two robust features of the underlying physics: (i) phase diffusion that is present in any condensate with number fluctuations and (ii) Josephson type tunneling that would be present in any well-defined two-mode system with contact between the modes. Both occur at times *before* our approximation methods cease to be valid.

Finally, the discussion in this section implies that our methods cannot quantitatively predict the amplitude for the generation of new momenta as in Sec. V D, since this process must rely on many-body integrability breaking through the approximations leading to MCTDHB or the two-mode model, the nature of which warrants further studies. For a quantitative prediction, physical integrability breaking terms [75,80] will be added in the future. Turning the argument around, our results also present clear evidence that the MCTDHB in one spatial dimension does not preserve the many-body integrability of the LL model when applied to it.

VII. VELOCITY DEPENDENCE OF ATOM TRANSFER

In Sec. V C we had discussed that atom-transfer during a collision of solitons can lead to dramatic consequences for the final many-body quantum state. In the framework of the two-mode model (7), this transfer is due to nonadiabatic effects from the temporal change of the Hamiltonian $\hat{H}$ in (9). These changes arise from the coefficients J, $\bar{J}$, and $\bar{D}$ that depend on soliton separation $d(t)$.

We thus expect the number distribution in soliton collisions to significantly depend on the collision velocity. However, for very slow collisions, we expect the two-mode model quantum state to adiabatically follow the changes in parameters, and thus return to the initial state after the collisions, which is what is seen in Fig. 9(a). For larger velocities, Fig. 9 shows that the number transfer depends nontrivially on the collision velocity.

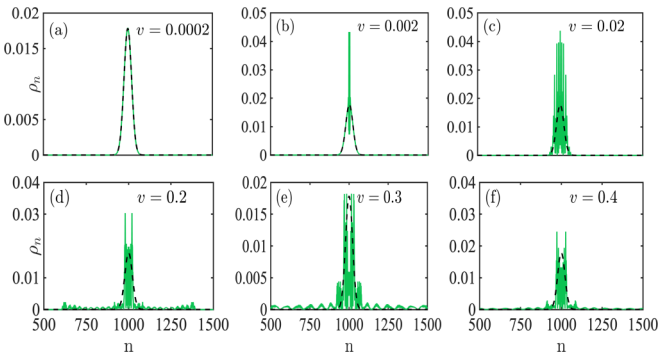

FIG. 9. Atom number distribution ρ_n in a single soliton from the TMM before the collision (black dashed) and after (green solid). The scenario is the same as in Fig. 6, except that we vary the velocity of each soliton v as indicated in the panels. All cases are for repulsive initial phases $\varphi = \pi$ and brought to collision at $t_{\rm coll} = 80$ or later (after fragmentation) by adjusting $d_{\rm ini}$.

In principle, we could expect a second regime without a change in the number distribution: for very fast collisions the quantum many-body state should stay unchanged, since a very short collision yields a sudden, impulsive change in Hamiltonian parameters with equally sudden return to the initial Hamiltonian. However, we find that, for collisions fast enough for that, there is sufficient kinetic energy for solitons to overcome their interactions even in the repulsive case. Since left and right soliton modes thus overlap at the collisions, results will be unreliable.

For repulsive collisions before fragmentation, we find no changes in the number distribution regardless of velocity.

VIII. SOLITON DECOHERENCE AT NONZERO TEMPERATURE AND DISCUSSION OF EXPERIMENTS

We will now discuss how the predictions of the other sections are consistent with existing experiments on soliton trains and their interactions and can further answer a variety of hitherto open questions.

Our analytical model (17) predicts a fragmentation time of $t_{\rm frag} = 877$ ms for the TSE [10] assuming $T \approx 0$ and $N_{\rm sol} = 28000$, $a_s = -0.57a_0$, and $\omega_\perp = (2\pi)254$ Hz. This is substantially beyond the experimentally covered range of collision times $t_{\rm coll} < 30 \ldots 320$ ms. However, it is comparable with the initial preparation time $t_{\rm prep}$, which exceeds 750 ms. It takes that long in the experiment to adiabatically split the condensate and then adjust the interaction's strength from its initial repulsive value to the final attractive one. Throughout all this time, phase diffusion will already be active. It is thus likely that TSE collisions already *begin* in a phase diffused and fragmented state. This is consistent with the experimental observation that collisions are indicative of all phases in $[0, 2\pi)$; see our discussion at the beginning of Sec. V B. Once *in situ* observation has collapsed a certain soliton pair onto a specific relative phase, the subsequent time is too short for refragmentation and thus further collisions are consistent with that initially chosen mean-field relative phase.

To investigate the onset of fragmentation and its dynamics, $t_{\rm frag}$ should be reduced. Larger solitons or stronger interactions could be problematic due to losses, but one can employ higher temperatures or noise, as we show now. Finite temperature condensates can straightforwardly be modeled using the TWA [50]. Returning to the scenario of two noncolliding solitons identical to the one in Fig. 3, we show the temperature dependence of the fragmentation timescale in Fig. 10(a). The data is fit by $t_{\rm frag} \sim T^{-0.44}$. The additional spread of intersoliton phases due to the interaction with hotter uncondensed atoms thus significantly accelerates fragmentation. It is useful that $t_{\rm frag}$ spans the full range, from longer than most experiments ($\sim$1 s) down to shorter than many ($\sim$50 ms), within the relevant temperature range from a few nK to typical condensation temperatures of a few 100 nK. This opens a convenient window on the intricate many-body dynamics described in earlier sections, while still permitting one to avoid fragmentation for interferometric applications.

In the light of accelerated fragmentation due to thermal atoms, let us now also revisit the MSE [9]. We performed a 3D simulation of that experiment, using a single trajectory of TWA at finite temperature. Column densities as shown in

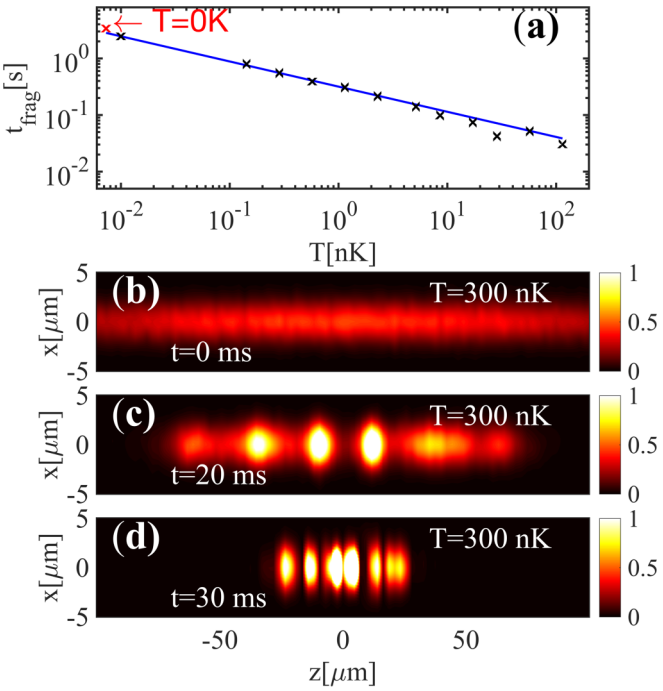

FIG. 10. (a) Fragmentation time as a function of temperature $T > 0$ from TWA, for soliton parameters matching the multisoliton experiment [9]. The solid line is the fit $t_{\rm frag} = 0.32$ s $(T/{\rm nK})^{-0.44}$. (b),(c) Normalized column density from single TWA trajectory with thermal noise matching $T_{\rm eff} = 300$ nK; see also Supplemental Material movies [83] (black, zero; bright, high). Lower effective temperatures would not reproduce the initial fluctuations visible in the experiment, (b), nor the time of first formation of solitons in (c). Panel (d) demonstrates the complete soliton train at later time. An initial uncondensed component with effective temperature $T_{\rm eff} = 300$ nK would cause fragmentation on a 10 ms timescale, according to panel (a).

Fig. 10, that correspond to an image of the atomic cloud taken from the side, should roughly agree with those in [9], regarding characteristic features like amplitude of fluctuations or formation time of solitons. This is only possible by assuming relatively high initial effective temperatures $T_{\rm eff} \gtrsim 300$ nK. Referring to Fig. 10(a), for which $N_{\rm sol}$ and U_0 are matching this experiment, we then read off an expected fragmentation time of the order of $t_{\rm frag} = O(10$ ms), compared to $t_{\rm frag} \approx 2$ s at $T = 0$, based on $N_{\rm sol} = 40000$, $a_s = -0.18a_0$, and $\omega_\perp = (2\pi)346$ Hz. Only under these conditions can the entire soliton train fragment before the moment of first collisions, about $t_{\rm coll} = 15$ ms after soliton formation and $t_{\rm coll} + t_{\rm form} = 25$ ms after experiment initiation. Subsequent collisions would then be expected to have predominantly repulsive character as experimentally observed.

A hot initial condensate is an even more appropriate starting point for the earlier experiments that reported mainly repulsion in soliton trains [6,8], which first went through collapse instabilities causing substantial nonequilibrium heating [84–87]. In contrast, accelerated fragmentation due to environmental noise does not occur during collisions in the TSE, since soliton creation there initially follows a slow adiabatic procedure, with substantially less heating than during a collapse or instability.

Another prediction of this article that contributes to an overall picture of predominantly repulsive collisions due to quantum effects is the acceleration of fragmentation if there are attractive collisions (possibly initially and rare), as discussed in Sec. V A. While most of the experiments discussed would not have had the sensitivity to detect the superelastic effects predicted in Sec. V C, these should play a role in the TSE setting [10], and could possibly be observed with minor improvements of the sensitivity there.

Finally, the dynamic choice of a fixed relative phase in the TSE would be related to measurement induced collapse of the many-body wave function, according to the picture here. The possibility to continuously and nondestructively infer soliton collisions properties in a setup such as [10] opens the door wide for explorations of the interplay between the highly entangling many-body collision dynamics predicted in earlier sections and continuous, controlled wave-function collapse by measurements.

IX. COMPARISON OF METHODS

Even though TWA formally should be valid only closer to a mean-field situation, it agrees with MCTDHB on a large number of features in postfragmentation soliton collisions: (i) the fact that these are a mixture of repulsive and attractive ones, with more repulsive ones, (ii) the qualitative shape of mean density, and (iii) the re-coherence features evident in Figs. 6(f) and 6(h). We would like to place this observation in the context of the discussion in [37,68,88–90].

The present work demonstrates fruitful complementarity of all three methods employed: thermal effects in Fig. 10 are naturally treated in the TWA. TWA, however, is troubled by controlled collisions as in Fig. 6, since it must also include random velocities and positions of the solitons. The latter yield an uncertain $t_{\rm coll}$, blurring collisions when averaging. These fluctuations are inherent in the quantum dynamics of the center-of-mass (c.m.) wave function of solitons [90,91], but not included in MCTDHB with two orbitals. In contrast to [90] we consider this a positive feature: the absence of c.m. diffusion in MCTDHB simplifies studies of collisions. At the same time agreement where possible between TWA and MCTDHB and consistency with our physical mechanisms makes us confident that TWA and MCTDHB have captured the essential many-body dynamics of phase diffusion or fragmentation correctly. To pinpoint the underlying basic physics, on the other hand, reduction to the simple two-mode model has been most useful.

X. CONCLUSIONS AND OUTLOOK

We comprehensively consider two crucial beyond-mean-field features in soliton collisions. The first, phase diffusion, is clearly linked to the fragmentation of soliton trains reported in [26]. Phase diffusion occurs whenever the atom number within one soliton is uncertain. Since we cannot allocate a well-defined intersoliton phase without allowing an uncertain atom number due to their complementarity, it is thus unavoidable in principle that fragmentation eventually invalidates mean-field theory for soliton collisions. In practice, the

relevant timescale, which we have evaluated analytically, can be fairly large at very low temperatures.

We have further shown that the timescale is shortened significantly through the presence of uncondensed atoms, whether these arise from nonzero temperature or nonequilibrium dynamics. Through this acceleration of fragmentation, beyond mean-field effects can explain predominantly repulsive interactions of solitons in trains generated after some nonequilibrium instability dynamics [6,8,9]. Nonetheless, we still expect soliton collisions under more controlled conditions as in [10] to adhere to mean-field theory.

We have additionally suggested the generation of entanglement between atom-number and postcollisions position and momentum through soliton collisions involving integrability breaking features of the underlying 3D physics. These features warrant further explorations, using either full-fledged 3D quantum field methods in a top-down approach or by explicitly including physical processes that break many-body integrability in effective 1D models.

ACKNOWLEDGMENTS

We gladly acknowledge the Max-Planck Society (Germany) for funding under the MPG-IISER partner group program, and interesting discussions with T. Busch, S. Cornish, M. Davis, S. Gardiner, J. Hope, and C. Weiss. A.S.R. acknowledges the Department of Science and Technology (DST), New Delhi, India, for the INSPIRE Fellowship No. IF160381.

APPENDIX A: DIMENSIONLESS UNITS

The 1D GPE (2) can be written in a dimensionless form, by transforming wave function, space, and time co-ordinates, respectively, as $\tilde{\phi} = \phi\sqrt{L}$, $\tilde{x} = \frac{x}{L}$, and $\tilde{t} = \frac{t}{T}$, where tilded quantities are dimensionless. The scales are $T = \frac{mL^2}{\hbar}$ and $L = \frac{2\hbar^2}{m|U_0|N_{\rm sol}}$, where the latter is chosen to yield a dimensionless soliton size $\tilde{\xi} = 1$ for our most commonly used parameters. After untilding all variables except $\tilde{U}_0 = \frac{T}{L\hbar}U_0$, the dimensionless GPE is then

$$i\frac{\partial}{\partial t}\phi(x,t) = \left[-\frac{1}{2}\frac{\partial^2}{\partial x^2} + \tilde{U}_0|\phi(x,t)|^2\right]\phi(x,t). \tag{A1}$$

APPENDIX B: POSTCOLLISION VELOCITY AFTER ATOM TRANSFER

After solving Eq. (21) and Eq. (22), the outgoing momenta as a function of $N_{\rm sol}$, a, m, and χ are as follows:

$$|p_+| = \frac{\sqrt{a - N_{\rm sol}}\sqrt{a^2 m\chi - p_0^2 N_{\rm sol}}}{\sqrt{aN_{\rm sol} + N_{\rm sol}^2}}. \tag{B1}$$

Thus the resultant velocity takes the form $v(n) = \frac{p_+}{m}$, which is a function of $N_{\rm sol}$. These are shown with the magenta line in panels (f) and (h) in Fig. 6.

[1] C. J. Pethick and H. Smith, *Bose-Einstein Condensation in Dilute Gases* (Cambridge University Press, Cambridge, UK, 2002).
[2] F. Dalfovo, S. Giorgini, L. P. Pitaevskii, and S. Stringari, Rev. Mod. Phys. **71**, 463 (1999).
[3] Y. S. Kivshar and G. P. Agrawal, *Optical Solitons: From Fibers to Photonic Crystals* (Academic Press, San Diego, 2003).
[4] K. E. Strecker, G. B. Partridge, A. G. Truscott, and R. G. Hulet, New J. Phys. **5**, 73 (2003).
[5] L. Khaykovich, F. Schreck, G. Ferrari, T. Bourdel, J. Cubizolles, L. D. Carr, Y. Castin, and C. Salomon, Science **296**, 1290 (2002).
[6] K. E. Strecker, G. B. Partridge, A. G. Truscott, and R. G. Hulet, Nature (London) **417**, 150 (2002).
[7] B. Eiermann, T. Anker, M. Albiez, M. Taglieber, P. Treutlein, K.-P. Marzlin, and M. K. Oberthaler, Phys. Rev. Lett. **92**, 230401 (2004).
[8] S. L. Cornish, S. T. Thompson, and C. E. Wieman, Phys. Rev. Lett. **96**, 170401 (2006).
[9] J. H. V. Nguyen, D. Luo, and R. G. Hulet, Science **356**, 422 (2017).
[10] J. H. V. Nguyen, P. Dyke, D. Luo, B. A. Malomed, and R. G. Hulet, Nat. Phys. **10**, 918 (2014).
[11] A. L. Marchant, T. P. Billam, M. M. H. Yu, A. Rakonjac, J. L. Helm, J. Polo, C. Weiss, S. A. Gardiner, and S. L. Cornish, Phys. Rev. A **93**, 021604(R) (2016).
[12] A. L. Marchant, T. P. Billam, T. P. Wiles, M. M. H. Yu, S. A. Gardiner, and S. L. Cornish, Nat. Commun. **4**, 1865 (2013).
[13] P. Medley, M. A. Minar, N. C. Cizek, D. Berryrieser, and M. A. Kasevich, Phys. Rev. Lett. **112**, 060401 (2014).
[14] S. Lepoutre, L. Fouché, A. Boissé, G. Berthet, G. Salomon, A. Aspect, and T. Bourdel, Phys. Rev. A **94**, 053626 (2016).
[15] A. Boisse, G. Berthet, L. Fouche, G. Salomon, A. Aspect, S. Lepoutre, and T. Bourdel, Europhys. Lett. **117**, 10007 (2017).
[16] G. D. McDonald, C. C. N. Kuhn, K. S. Hardman, S. Bennetts, P. J. Everitt, P. A. Altin, J. E. Debs, J. D. Close, and N. P. Robins, Phys. Rev. Lett. **113**, 013002 (2014).
[17] P. J. Everitt, M. A. Sooriyabandara, M. Guasoni, P. B. Wigley, C. H. Wei, G. D. McDonald, K. S. Hardman, P. Manju, J. D. Close, C. C. N. Kuhn *et al.*, Phys. Rev. A **96**, 041601(R) (2017).
[18] S. E. Pollack, D. Dries, M. Junker, Y. P. Chen, T. A. Corcovilos, and R. G. Hulet, Phys. Rev. Lett. **102**, 090402 (2009).
[19] T. Mežnaršič, T. Arh, J. Brence, J. Pišljar, K. Gosar, Ž. Gosar, R. Žitko, E. Zupanič, and P. Jeglič, Phys. Rev. A **99**, 033625 (2019).
[20] J. P. Gordon, Opt. Lett. **8**, 596 (1983).
[21] T. P. Billam and C. Weiss, Nat. Phys. **10**, 902 (2014).
[22] U. Al Khawaja, H. T. C. Stoof, R. G. Hulet, K. E. Strecker, and G. B. Partridge, Phys. Rev. Lett. **89**, 200404 (2002).
[23] B. J. Dąbrowska-Wüster, S. Wüster, and M. J. Davis, New J. Phys. **11**, 053017 (2009).
[24] L. D. Carr and J. Brand, Phys. Rev. Lett. **92**, 040401 (2004).

[25] L. Salasnich, A. Parola, and L. Reatto, Phys. Rev. Lett. **91**, 080405 (2003).
[26] A. I. Streltsov, O. E. Alon, and L. S. Cederbaum, Phys. Rev. Lett. **106**, 240401 (2011).
[27] M. Lewenstein and L. You, Phys. Rev. Lett. **77**, 3489 (1996).
[28] M. Albiez, R. Gati, J. Fölling, S. Hunsmann, M. Cristiani, and M. K. Oberthaler, Phys. Rev. Lett. **95**, 010402 (2005).
[29] N. G. Parker, A. M. Martin, S. L. Cornish, and C. S. Adams, J. Phys. B: At. Mol. Opt. Phys. **41**, 045303 (2008).
[30] F. M. Mitschke and L. F. Mollenhauer, Opt. Lett. **12**, 355 (1987).
[31] R. J. Dodd, M. Edwards, C. J. Williams, C. W. Clark, M. J. Holland, P. A. Ruprecht, and K. Burnett, Phys. Rev. A **54**, 661 (1996).
[32] N. G. Parker, A. M. Martin, C. S. Adams, and S. L. Cornish, Physica D **238**, 1456 (2009).
[33] N. G. Parker, S. L. Cornish, C. S. Adams, and A. M. Martin, J. Phys. B: At. Mol. Opt. Phys. **40**, 3127 (2007).
[34] V. Y. F. Leung, A. G. Truscott, and K. G. H. Baldwin, Phys. Rev. A **66**, 061602(R) (2002).
[35] O. E. Alon, A. I. Streltsov, and L. S. Cederbaum, Phys. Rev. A **77**, 033613 (2008).
[36] A. I. Streltsov, O. E. Alon, and L. S. Cederbaum, Phys. Rev. Lett. **100**, 130401 (2008).
[37] O. E. Alon and L. S. Cederbaum, Chem. Phys. **515**, 287 (2018).
[38] K. Sakmann, A. I. Streltsov, O. E. Alon, and L. S. Cederbaum, Phys. Rev. A **89**, 023602 (2014).
[39] G. C. Katsimiga, S. I. Mistakidis, G. M. Koutentakis, P. G. Kevrekidis, and P. Schmelcher, Phys. Rev. A **98**, 013632 (2018).
[40] G. C. Katsimiga, S. I. Mistakidis, G. M. Koutentakis, P. G. Kevrekidis, and P. Schmelcher, New J. Phys. **19**, 123012 (2017).
[41] A. I. Streltsov, O. E. Alon, and L. S. Cederbaum, Phys. Rev. A **80**, 043616 (2009).
[42] J. Grond, T. Betz, U. Hohenester, N. J. Mauser, J. Schmiedmayer, and T. Schumm, New J. Phys. **13**, 065026 (2011).
[43] S. Krönke, J. Knörzer, and P. Schmelcher, New J. Phys. **17**, 053001 (2015).
[44] G. C. Katsimiga, G. M. Koutentakis, S. I. Mistakidis, P. G. Kevrekidis, and P. Schmelcher, New J. Phys. **19**, 073004 (2017).
[45] J. G. Cosme, M. F. Andersen, and J. Brand, Phys. Rev. A **96**, 013616 (2017).
[46] K. Sakmann, A. U. J. Lode, A. I. Streltsov, O. E. Alon, and L. S. Cederbaum, Openmctdhb v2.3, http://OpenMCTDHB.uni-hd.de.
[47] M. J. Steel, M. K. Olsen, L. I. Plimak, P. D. Drummond, S. M. Tan, M. J. Collett, D. F. Walls, and R. Graham, Phys. Rev. A **58**, 4824 (1998).
[48] A. Sinatra, C. Lobo, and Y. Castin, Phys. Rev. Lett. **87**, 210404 (2001).
[49] A. Sinatra, C. Lobo, and Y. Castin, J. Phys. B: At. Mol. Opt. Phys. **35**, 3599 (2002).
[50] P. Blakie, A. Bradley, M. Davis, R. Ballagh, and C. Gardiner, Adv. Phys. **57**, 363 (2008).
[51] M. R. Hush, A. R. R. Carvalho, and J. J. Hope, Phys. Rev. A **81**, 033852 (2010).
[52] J. F. Corney and M. K. Olsen, Phys. Rev. A **91**, 023824 (2015).
[53] A. Polkovnikov, Phys. Rev. A **68**, 033609 (2003).
[54] A. A. Norrie, R. J. Ballagh, and C. W. Gardiner, Phys. Rev. Lett. **94**, 040401 (2005).
[55] A. A. Norrie, R. J. Ballagh, and C. W. Gardiner, Phys. Rev. A **73**, 043617 (2006).
[56] A. A. Norrie, Ph.D. thesis, University of Otago, 2005.
[57] G. R. Dennis, J. J. Hope, and M. T. Johnsson, http://www.xmds.org/.
[58] G. R. Dennis, J. J. Hope, and M. T. Johnsson, Comput. Phys. Commun. **184**, 201 (2013).
[59] O. Penrose and L. Onsager, Phys. Rev. **104**, 576 (1956).
[60] P. B. Blakie and M. J. Davis, Phys. Rev. A **72**, 063608 (2005).
[61] A. I. Streltsov, K. Sakmann, O. E. Alon, and L. S. Cederbaum, Phys. Rev. A **83**, 043604 (2011).
[62] D. F. Walls and G. J. Milburn, *Quantum Optics* (Springer-Verlag, Berlin, 1994).
[63] M. T. Johnsson and S. A. Haine, Phys. Rev. Lett. **99**, 010401 (2007).
[64] S. Wüster, B. J. Dąbrowska-Wüster, S. M. Scott, J. D. Close, and C. M. Savage, Phys. Rev. A **77**, 023619 (2008).
[65] Y. Lai and H. A. Haus, Phys. Rev. A **40**, 844 (1989).
[66] Y. Lai and H. A. Haus, Phys. Rev. A **40**, 854 (1989).
[67] A. D. Martin and J. Ruostekoski, New J. Phys. **14**, 043040 (2012).
[68] K. Sakmann and M. Kasevich, Nat. Phys. **12**, 451 (2016).
[69] P. G. Kevrekidis, D. J. Frantzeskakis, R. Carretero-González, B. A. Malomed, G. Herring, and A. R. Bishop, Phys. Rev. A **71**, 023614 (2005).
[70] M. Lewenstein and B. A. Malomed, New J. Phys. **11**, 113014 (2009).
[71] B. Gertjerenken, T. P. Billam, C. L. Blackley, C. R. Le Sueur, L. Khaykovich, S. L. Cornish, and C. Weiss, Phys. Rev. Lett. **111**, 100406 (2013).
[72] R. V. Mishmash and L. D. Carr, Phys. Rev. Lett. **103**, 140403 (2009).
[73] J. B. McGuire, J. Math. Phys. **5**, 622 (1964).
[74] E. H. Lieb and W. Liniger, Phys. Rev. **130**, 1605 (1963).
[75] D. I. H. Holdaway, C. Weiss, and S. A. Gardiner, Phys. Rev. A **89**, 013611 (2014).
[76] J. Yu-Zhu, C. Yang-Yang, and G. Xi-Wen, Chin. Phys. B **24**, 050311 (2015).
[77] T. Kinoshita, T. Wenger, and D. S. Weiss, Nature (London) **440**, 900 (2006).
[78] S. Hofferberth, I. Lesanovsky, B. Fischer, T. Schumm, A. Imambekov, V. Gritsev, E. Demler, and J. Schmiedmayer, Nat. Phys. **4**, 489 (2008).
[79] S. Hofferberth, I. Lesanovsky, B. Fischer, T. Schumm, and J. Schmiedmayer, Nature (London) **449**, 324 (2007).
[80] I. E. Mazets, T. Schumm, and J. Schmiedmayer, Phys. Rev. Lett. **100**, 210403 (2008).
[81] K. Bongs, S. Burger, S. Dettmer, D. Hellweg, J. Arlt, W. Ertmer, and K. Sengstock, Phys. Rev. A **63**, 031602(R) (2001).
[82] L. Khaykovich and B. A. Malomed, Phys. Rev. A **74**, 023607 (2006).
[83] See Supplemental Material at http://link.aps.org/supplemental/10.1103/PhysRevA.101.043604 for movies of soliton train formation in a single TWA trajectory at $T = 0\,\mathrm{nK}$ and $T = 300\,\mathrm{nK}$.
[84] E. A. Donley, N. R. Claussen, S. L. Cornish, J. L. Roberts, E. A. Cornell, and C. E. Wieman, Nature (London) **412**, 295 (2001).

[85] S. Wüster, J. J. Hope, and C. M. Savage, Phys. Rev. A **71**, 033604 (2005).
[86] S. Wüster, B. J. Dąbrowska-Wüster, A. S. Bradley, M. J. Davis, P. B. Blakie, J. J. Hope, and C. M. Savage, Phys. Rev. A **75**, 043611 (2007).
[87] J. N. Milstein, C. Menotti, and M. J. Holland, New J. Phys. **5**, 52 (2003).
[88] P. D. Drummond and J. Brand, arXiv:1610.07633v1.
[89] K. Sakmann and M. Kasevich, arXiv:1702.01211v2.
[90] J. G. Cosme, C. Weiss, and J. Brand, Phys. Rev. A **94**, 043603 (2016).
[91] C. Weiss, S. A. Gardiner, and H.-P. Breuer, Phys. Rev. A **91**, 063616 (2015).